

ATATA: One Algorithm to Align Them All

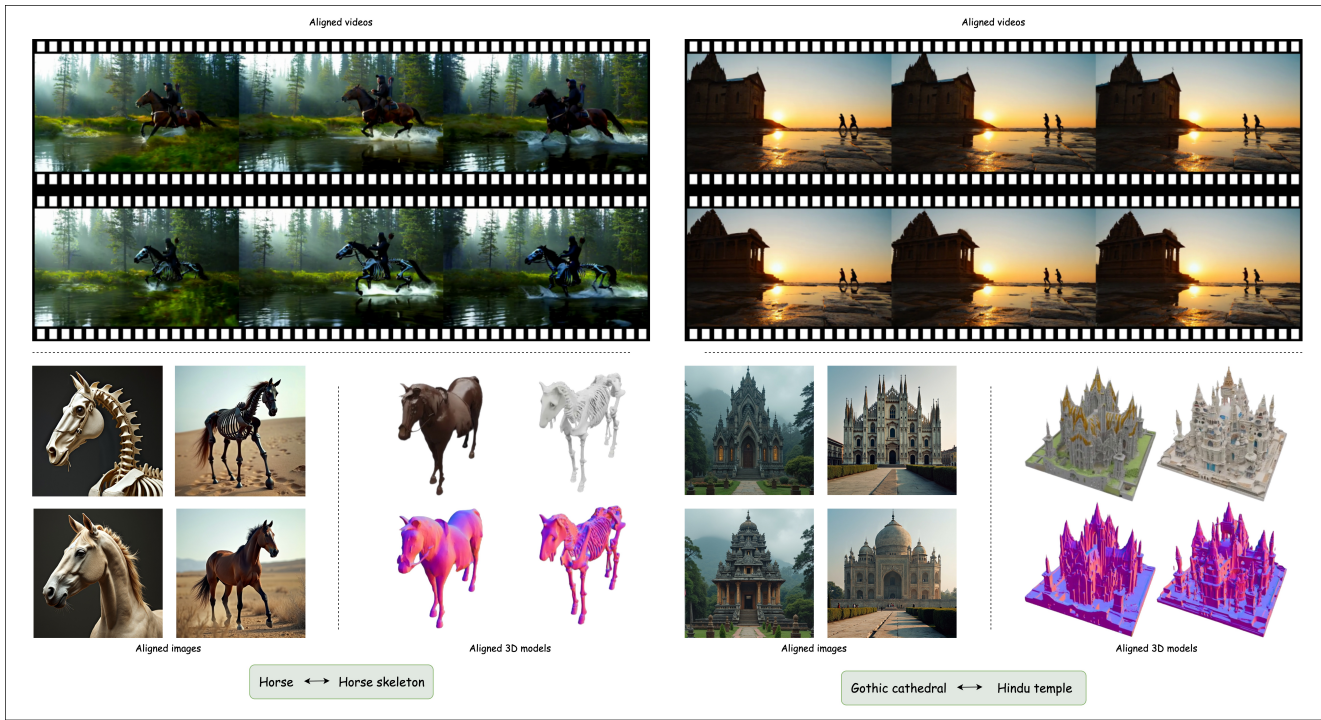
Boyi Pang^{1,*}Yurii Melnik²Savva Ignatyev^{2,*}Oleg Voynov²Vladimir Ippolitov^{2,*}Maksim Nakhodnov^{3, 4}Ramil Khafizov²Aibek Alanov^{3, 5}Xiaopeng Fan^{1,6,7 †}Peter Wonka^{8†}Evgeny Burnaev²*Equal contribution †Indicates the corresponding author ¹Harbin Institute of Technology²Applied AI Institute ³Fusion Brain ⁴MSU ⁵HSE University⁶The Peng Cheng Laboratory ⁷HIT Suzhou Research Institute ⁸KAUST

Figure 1. Visualization of generated images, videos, and 3D shapes using our method. The left pair is (horse animal, horse skeleton), the right pair is (gothic temple, hindu temple).

Abstract

We suggest a new multi-modal algorithm for joint inference of paired structurally aligned samples with Rectified Flow models. While some existing methods propose a codependent generation process, they do not view the problem of joint generation from a structural alignment perspective.

Recent work uses Score Distillation Sampling to generate aligned 3D models, but SDS is known to be time-consuming, prone to mode collapse, and often provides cartoonish results. By contrast, our suggested approach relies on the joint transport of a segment in the sample space, yielding faster computation at inference time. Our approach can be built on top of an arbitrary Rectified Flow model operat-

ing on the structured latent space. We show the applicability of our method to the domains of image, video, and 3D shape generation using state-of-the-art baselines and evaluate it against both editing-based and joint inference-based competing approaches. We demonstrate a high degree of structural alignment for the sample pairs obtained with our method and a high visual quality of the samples. Our method improves the state-of-the-art for image and video generation pipelines. For 3D generation, it is able to show comparable quality while working orders of magnitude faster. voyleg.github.io/atata/

1. Introduction

Images, videos, and 3D models are three important domains for generative AI. While users often employ AI to generate one sample at a time, there are many use cases where a user wants to generate a set of examples that are somehow related. Examples are personalization [1], where a user wants to have the same object or person appearing in multiple images or videos, or style consistent generation [13], where multiple samples should be generated in the same style.

In this paper, we address the topic of structurally aligned generation. The goal of structurally aligned generation is to generate multiple samples (images, videos, 3D models) that showcase different main objects, scenes, or environments, but with their semantically (structurally) corresponding parts aligned across spatial/temporal dimensions. This aligned generation comes in handy in generating virtual worlds for training and entertainment, where different objects and scene parts can be easily replaced across domains and "sewn up" into a new scene. It can also help in CAD and CAM applications for creating objects with interchangeable parts. For image and video editing, these tools can be useful for generating artistic effects, for example, transitions called matchcuts [38]. Finally, aligned generation methods can be useful for paired synthetic training data generation for image, video, and 3D, which can be later used to train editing models. While existing methods try to use editing for aligned generation [5, 21, 41], this biases the generation to construct samples that fit one of the descriptions better than the others.

Current methods for aligned generation fall into three categories: 1) Editing-based methods, which use the input sample defined by the first description and force the second sample to adopt its structure. 2) Zero-shot generation using large foundation models. Many large generative models like Nanobanana [12], QWEN [54], or FLUX [4] can generate a grid of semi-consistent images or 3D renders. 3) Native aligned generation. Some works solve the problem of the joint aligned generation, introducing some kind of interaction between the samples during generation. This includes joint generation up to some step in MatchDiffusion [38],

attention sharing [13], or embedding into a common latent space in A3D [19].

We propose a novel, highly generalizable, multi-modal method for structurally aligned generation. Inspired by A3D [19], we rethink the necessary properties of transitions between samples with regard to rectified flow field numerical integration and introduce additional constraints to the process, which are necessary for the algorithm's convergence. The method is theoretically applicable to any rectified flow model that operates on the structured latent space, which is demonstrated for images, videos, and 3D objects with minor implementation differences between them. The method requires only changing the inference loop of the flow model, without changing any other components of the pipeline, and does not depend on the specific domain. The main idea of the method is to perform joint inference for pairs of samples by moving them and the linear interpolations between them along the velocity field of the rectified flow model while preserving the interpolation structure. We additionally introduce joint co-guidance during the transport process aimed at ensuring the smoothness of the linear transitions between the samples. Unlike A3D [19], our method is inference-based and does not use SDS, which makes it orders of magnitude faster, allows for reaching state-of-the-art visual quality results without artifacts, and provides a notable variety of samples avoiding mode collapse. Unlike MatchDiffusion [38], our method optimizes for the plausibility of the linear transitions between samples, notably improving structural alignment. It also provides a flexible way to co-guide samples during the inference process.

In summary, we make the following contributions.

- We propose a new algorithm for joint paired inference with rectified flow models, which is based on velocity-guided transport of a segment in latent space, and provide a theoretical justification for it.
- We derive an analytical way to convert the rectified model velocity field into a velocity transport field for joint segment transport.
- We demonstrate that the proposed algorithm, combined with models trained on structured latents, produces highly structurally aligned samples for three modalities: images, videos, and 3D models.
- We obtain results on par with state-of-the-art, specifically trained methods on images and 3D models, and show superior state-of-the-art results on videos.

2. Related work

2.1. Image Generation and Editing

Image generation and editing have become central components of modern generative modeling, forming the foundation for controllable video and 3D synthesis. The

early approaches relied on Generative Adversarial Networks (GANs) [11, 17, 23] and Variational Autoencoders (VAEs) [25, 52], which were later surpassed by higher-quality diffusion-based methods such as DDPM [14] and Stable Diffusion [44]. The introduction of these models marked a significant step towards scalable text-to-image generation [42, 46, 48].

More recent progress in text-to-image modeling has been driven by the emergence of Rectified Flow [35] and Diffusion Transformers (DiT) [39], which underpin several state-of-the-art systems, including FLUX.1 [4], Stable Diffusion 3 [9], and Qwen-Image [54]. The advantageous properties of these frameworks—such as stable training and expressive conditioning—have enabled the natural extension of diffusion-based methods to the image editing domain, as demonstrated by [26, 41, 45].

2.2. Video Generation and Editing

Video-based models are still far behind image-based models due to computational requirements and data scarcity [15, 53]. Existing video editing methods could be split into two groups, where the first relies on training-free modification of video generation models and the second relies on training a separate architecture for editing.

Training-free editing approaches are easy and fast to adopt for the most recent models. One bright representative of this family is MatchDiffusion [37], which relies on joint and disjoint diffusion stages, balancing between visual coherence and semantic divergence.

Methods requiring training allow more versatile and fine-grained edits. Among these methods, VACE [20] stands out for its possibility to use a diverse set of conditions: from inpainting to depth and motion preservation. Another work, LucyEdit [8], focuses on purely textual edits and special “trigger” words, allowing control of the granularity of edits.

2.3. 3D Generation and Editing

Alongside progress in image and video generation, 3D object and scene synthesis have also advanced significantly. Unlike 2D domains, where large-scale datasets enable highly generalizable models [4, 54], limited 3D data availability has led researchers to exploit 2D priors from pre-trained models—either through multi-view generation with subsequent reconstruction [10, 18, 31, 47, 49] or through score distillation from 2D diffusion models ([34, 36, 40]). More recently, diffusion and flow matching models that operate directly in a 3D latent space have become competitive [27, 57, 59]. These methods fall into two main groups: those using structured voxel-based latents [55, 57, 59] and unstructured latents [27, 28, 62]. While unstructured latents are more computationally efficient, structured ones offer better interpretability—an advantage we build upon in our work. The landscape of 3D editing methods is parallel

to that of 3D generation. Early progress relied on the use of 2D priors: either via score distillation [7, 33, 63, 64] or via multi-view diffusion [5, 6, 29]. Recently, methods that operate directly in 3D latent space have enabled the design of editing systems that also operate in 3D space [32, 57, 60]. However, they still have limited generalization ability due to data scarcity, so 2D-based methods remain a strong baseline for this task.

2.4. Joint Generation of Consistent Objects

Recent advances in generative modeling have shown that it is possible to simultaneously generate multiple objects with shared properties. These shared properties can be of different nature: [30, 61] exploit synchronization mechanisms to produce multiple views of a scene that can subsequently be merged into a panorama, [1] proposed a procedure to generate a set of images with consistent identity. The joint generation of geometrically aligned 3D assets remains more challenging, and the existing solution relies on an iterative, time-consuming SDS-based A3D algorithm [19]. Its core idea is to enforce smooth transitions between generations during the generation process. MatchDiffusion [38] proposes a training-free approach to joint generation that merges two trajectories before a threshold timestep, but we found that this trajectory merging alone is not sufficient to achieve proper structure alignment, motivating our contributions.

3. Preliminaries

3.1. Flow Matching

Recently, there emerged a tendency in the community to switch from the denoising diffusion models to simpler and more effective Rectified Flow [35] models. Given a distribution X_0 and a sample from it $x_0 \sim X_0$, the initial distribution is transformed into the “noised” version via linear interpolation with $\epsilon \sim \mathcal{N}(0, \mathbf{I})$, where $t \in [0, 1]$.

$$x_t = (1 - t)x_0 + t\epsilon \quad (1)$$

Then a transformer model is trained to directly regress the velocity field $v_\theta(x_t, t)$ by minimi

$$\mathcal{L}(\theta) = \mathbb{E}_{t, x_0 \sim X_0, x_1 \sim X_1} \left[\|v - v_\theta(x_t, t)\|^2 \right]. \quad (2)$$

4. Method

Multiple works [3, 19, 24] imply the importance of two requirements for learning the transitions between samples, which lead to the generation of the semantically aligned objects: 1) Transitions between the aligned objects should provide plausible and realistic samples. 2) Transitions should be smooth (or have a bounded Lipschitz constant). In this

section, we analyze these requirements and suggest a principled algorithm for joint inference with rectified flow models, which can be combined with an arbitrary pre-trained model operating on the set of structured latents.

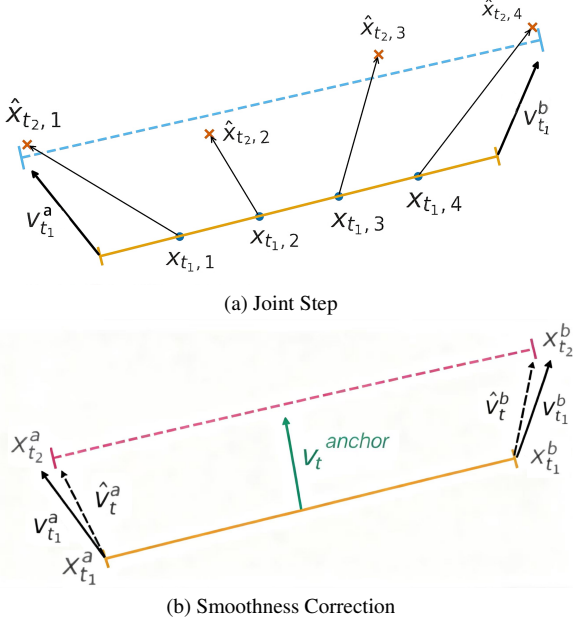


Figure 2. Method

4.1. Joint Inference with Rectified Flow Models

Flow-matching models use time discretization to approximate trajectories along the velocity vector field $v_\Theta(x_t, t, c)$, which is parameterized by a neural network. Given a text embedding c and starting with a sample $x \sim \mathcal{N}(0, \mathbf{I})$ taken from a Gaussian noise distribution, the sample x_{t_1} at time step t_1 can be used to calculate x_{t_2} (where $t_1 > t_2$) with the following update rule:

$$x_{t_2} = x_{t_1} + (t_2 - t_1)v_\Theta(x_{t_1}, t_1, c) \quad (3)$$

Let c^a, c^b be two text embeddings and x^a, x^b be the sample variables corresponding to a pair of objects a and b . We initialize x^a and x^b with the same value. Instead of transporting them independently, we want to do it jointly to improve the plausibility of the transitions between them. To achieve this, we consider transporting a distribution of samples on the line segment $[x^a, x^b] = \{(1-\alpha)x^a + \alpha x^b \mid \alpha \in [0, 1]\}$ defined by some density function $p(\alpha)$. Thus, we shift from transporting individual samples to transporting probability distributions, while preserving the linear structure of these distributions.

To define the update rule for joint transport, we represent the samples distributed on the line segment with the density $p(\alpha)$ by a set of weighted samples evenly distributed across the segment $\{x_{t,i} = (1 - \alpha_i)x_t^a + \alpha_i x_t^b \mid$

$i = 1, \dots, k\}$ with the respective weighting factors $p(\alpha_i)$. Given the segment $[x_{t_1}^a, x_{t_1}^b]$ we update it to the segment $[x_{t_2}^a, x_{t_2}^b]$ in two steps. First, we update each point $x_{t_1,i}$ to $\hat{x}_{t_2,i}$ individually using the rule in Equation 3 and the interpolated text embedding $c_i = (1 - \alpha_i)c^a + \alpha_i c^b$. While the points $\{x_{t_1,i} \mid i = 1, \dots, k\}$ by definition always lie on a single line in high-dimensional space there is, generally speaking, no such guarantee for the updated points $\{\hat{x}_{t_2,i} \mid i = 1, \dots, k\}$. That is why we restore the linear structure of the distribution by solving a linear regression problem in Equation 4, minimizing \mathcal{L} w.r.t. $x_{t_2}^a$ and $x_{t_2}^b$.

$$\begin{aligned} \mathcal{L}(x_{t_2}^a, x_{t_2}^b) &= \sum_{i=1}^k p(\alpha_i) \|x_{t_2,i} - \hat{x}_{t_2,i}\|_2, \\ \hat{x}_{t_2,i} &= x_{t_1,i} + (t_2 - t_1)v_\Theta(x_{t_1,i}, t_1, c_i) \\ x_{t_2,i} &= (1 - \alpha_i)x_{t_2}^a + \alpha_i x_{t_2}^b \end{aligned} \quad (4)$$

This regression problem has an explicit solution. We define:

Then the optimal endpoints are:

$$x_{t_2}^a = \frac{c_{11}d_0 - c_{01}d_1}{\Delta}, \quad x_{t_2}^b = \frac{c_{00}d_1 - c_{01}d_0}{\Delta}, \quad (5)$$

The described approach enables a rapid update of the distribution parameters, thereby avoiding the slow gradient-based optimization. Finally, we can define the velocities of the parameters of the probability distribution (boundary points of the segment $x_{t_2}^a$ and $x_{t_2}^b$): The scheme of the joint update is shown in Figure 2a.

$$v_{t_1}^a = \frac{x_{t_2}^a - x_{t_1}^a}{t_2 - t_1} \quad v_{t_1}^b = \frac{x_{t_2}^b - x_{t_1}^b}{t_2 - t_1} \quad (6)$$

In the presented way, we transform the transport velocity field for samples into the joint transport velocity field for probability distributions supported by the segments in the sample space. In practice, we found it important to use the density $p(\alpha)$ centered around the midpoint during the early iterations and gradually shifted towards a uniform distribution.

4.2. Smoothness regularization

The second aspect is the need for smooth transitions between the two objects. For linear transitions, the "speed" of transition does not depend on the point and is always the same: $\frac{dx_t}{d\alpha} = \frac{d}{d\alpha}((1 - \alpha)x_t^a + \alpha x_t^b) = x_t^b - x_t^a$. Thus, regularizing the "speed" of transition is the same as regularizing the norm $\|x_t^b - x_t^a\|_2$ of the segment $[x_t^a, x_t^b]$. Since we initialize x^a and x^b with the same value, the segment norm is zero in the beginning, and over time it diverges, resulting in different, but structurally aligned samples.

The derivative of the L^2 norm of the segment can be written as

$$\frac{d\|x^b(t) - x^a(t)\|_2}{dt} = \frac{\langle v^b(t) - v^a(t), x^b(t) - x^a(t) \rangle}{\|x^b(t) - x^a(t)\|_2}, \quad (7)$$

where $\langle \cdot, \cdot \rangle$ is the dot product. We observe that in the cases where we see the severe misalignment between the samples, it usually correlates with the rapid growth of the segment norm during the early iterations of the inference. We can see that this derivative depends on the difference between the velocities of the endpoints of the segment $v^b - v^a$. Thus, minimizing the derivative can be achieved by minimizing this expression or making the velocities of the distribution parameters closer to each other. One particular way to achieve this is to correct the velocities by pulling them closer to some specific *anchor* velocity v^{anchor} (Equation 8)

$$\hat{v}_t^a = w_t v_t^{anchor} + (1-w_t) v_t^a \quad \hat{v}_t^b = w_t v_t^{anchor} + (1-w_t) v_t^b \quad (8)$$

The choice of v^{anchor} is important - the anchor velocity vector should point at the "denoising" direction for all the points on the segment in order not to break the noise schedule of the samples. One possible solution for this task would be to choose $v_t^{anchor} = \frac{v_t^a + v_t^b}{2}$. Though our experiments show that this solution is suboptimal, probably because these two endpoint velocities often have conflicting directions. Our suggested solution is to choose v^{anchor} as a predicted velocity (Equation 9) for the midpoint of the segment.

$$v_t^{anchor} = v_\Theta\left(\frac{x_t^a + x_t^b}{2}, t, \frac{c^a + c^b}{2}\right) \quad (9)$$

Note that such choice of v^{anchor} is essentially inseparable from the approach presented in Section 4.1 serving as a "correction" to the formulated velocity field, because for the proper inference $\frac{x_t^a + x_t^b}{2}$ should be a plausible sample from the noised distribution at the timestep t which requires taking into account the velocities for the intermediate points of the segment. The scheme for the smoothness correction mechanism is shown in Figure 2b. We observe that choosing the moderate schedule for the values w_t with the emphasis on early iterations does not lead to the degradation of the final samples compared to the "base" rectified flow method.

5. Experiments

We show the universality of our method for joint aligned generation by applying it to three major domains for generative modeling: images, 3D, and video. We select three state-of-the-art rectified flow pre-trained models, which operate on structured latents: voxels, pixels, and video frames. We modify the inference loops of these three models in a self-contained way, which requires only minor differences between the models. We do not change model weights or any other parts of the pipeline.

We use two types of methods as competitors i) joint generation methods, which produce paired output at sin-

gle inference (A3D [19], MatchDiffusion [38]) ii) editing-based methods which take an independently generated sample from the first prompt *source* and complement the pair by editing it with another prompt from the pair (RF-Inversion [45], VACE [21], and MVEdit [5]).

Metrics: We use multiple metrics to evaluate the degree of structural alignment between the samples and consistency between the samples and the corresponding textual descriptions.

Modality agnostic metrics are based on the evaluation of the sample "projections" to the 2D image space (multi-view images, video frames). **DIFT alignment score** was introduced in A3D [19] as a way to measure structural similarity between two salient objects on a pair of images. It works by building a dense grid of 2D points on the source image and finding the corresponding point for each point in the grid using the DIFT [50] method. The pairwise distance between the points is averaged. Finally, the metric is calculated in the reverse direction and averaged one more time. When calculating the DIFT Score, we use the Grounded SAM [43] segmentation model to focus on the foreground object to avoid matching the background. In the recent work SPIE [2] L_1 distance (or equivalently, MAE mean squared error) between the **depth** maps extracted from the image pair was shown to be an effective proxy metric for structural alignment. We extract depth maps for evaluation using the Depth Anything V2 model [58]. We also employ the widely-used **CLIP Score** to estimate how well each prompt fits the corresponding 2D image by calculating the similarity between the prompt embedding and image embedding. On par with CLIP, we use specific subcriteria from the MLLM [16] method to evaluate image-prompt alignment.

Video metrics are specifically designed to evaluate the qualities of videos. The temporal consistency of the videos is evaluated by calculating the similarity between the **DINO** features of neighboring frames for the edited video. To assess the overall quality of the videos, we use a **VLM** score [22] to evaluate the overall quality, prompt alignment, and preservation of the details of the source video.

3D metrics. We use **GPTEval** [56], a VLM-based method to evaluate the quality of 3D objects, including geometry, texture, and prompt consistency.

5.1. Images

We build our joint image generation pipeline on top of the widely used FLUX.1-dev [4], which is known for the excellent quality of text-to-image generation. For the consistency with 3D experiments, we use the set of object pairs from A3D [19] with short prompts. We compare with two editing-based methods, RF-Inversion [45], which is a flow-inversion training-free method, and instruction-based Qwen-Image-Edit [41, 54]. To obtain *source* editing-free samples, we use FLUX.1-dev model. We rewrite prompts



(a) dog, robot

(b) gopher, kangaroo

(c) spider, octopus

(d) amphitheatre, stadium

Figure 3. Visualization of geometry preservation between two generated images. For each example, two images are blended into one with a blending coefficient α (column) that depends on the column index, increasing from 0 (left side) to 1 (right side). With such blending, we show that not only geometry is preserved, but also that smooth transitions between two generations are enabled.

Table 1. 2D Metrics.

	CLIP \uparrow	DIFT distance \downarrow % of object size	Depth L1 \downarrow distance	MLLM-based \uparrow score
Qwen	24,10	11,33	37,64	89,60
RF_Inversion	23,36	8,62	28,50	83,07
Ours	23,23	6,44	26,83	83,33

Table 2. GPTEval 3D Metrics.

	GPTEval3D, % of comparisons where our method is preferred					
	Text-asset alignment	3D plausibility	Text-geometry alignment	Texture details	Geometry details	Overall quality
vs. MVEdit	66,94	68,04	67,09	61,44	72,29	62,15
vs. LucidDreamer	47,29	64,06	39,64	23,44	37,09	40,28
vs. A3D	42,94	63,72	30,85	26,17	30,37	51,22

Table 3. Other 3D Metrics.

	CLIP \uparrow	DIFT distance \downarrow % of object size		Time \downarrow
		5,45	40 min	
MVEdit	27,10	5,45	40 min	
LucidDreamer	26,40	11,29	2 h	
A3D	27,69	5,82	2 h	
Ours	28,29	6,98	1 min	

into instructions for Qwen-Image-Edit, asking it to change the content of the source image so that the geometry and background are preserved. For image pair evaluation, we use DIFT Score, Depth Structural Score, CLIP Score, and MLLM Score. The quantitative results are presented in the Table 1. Our method notably improves over RF-Inversion in terms of structural alignment metrics. While Qwen demonstrates a superior understanding of user instructions, it lags far behind in structural alignment score, which makes it unsuitable for this particular problem.

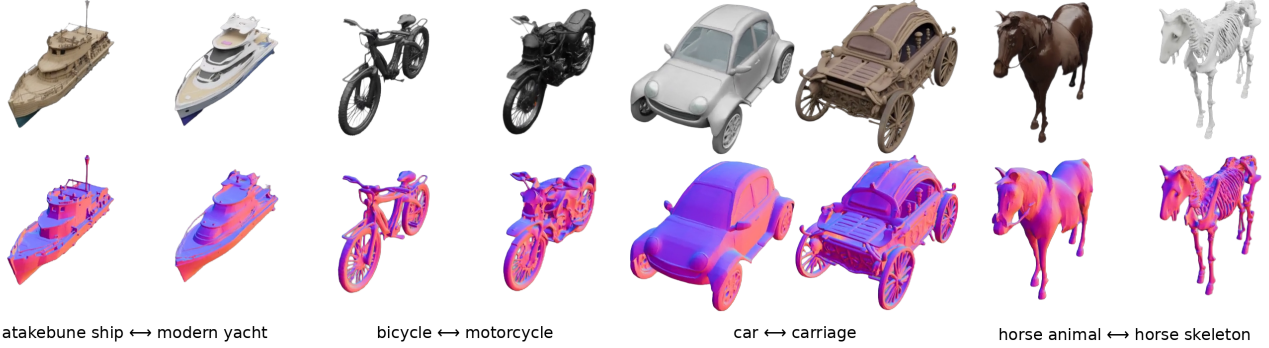
Our method can be used to seamlessly combine parts of the samples from parallel domains. We demonstrate it by changing the α blending coefficient across the horizontal axis for the pairs of images in Figure 3.

5.2. 3D Shapes

For the joint 3D object generation task, we build on top of the Trellis [57] text-to-3D method. The Trellis pipeline consists of two parts: *Structure Generation* operating on dense voxels and *Structured Latents Generation* working with a sparse latent representation. To generate geometrically aligned 3D models, we modify the inference loop for the rectified flow model in the first part of the pipeline, leaving everything else intact. Because the Trellis model was primarily trained on detailed text descriptions, this creates a distributional shift with the short prompts used for the A3D [19] evaluation. Therefore, we rewrite the short prompts into more detailed descriptions using GPT-

5. We compare our method with editing-based methods (MVEdit [5], LucidDreamer [34]) and with the joint generation method A3D. The source 3D models for the editing-based methods are obtained using the generative pipelines associated with each method. For evaluation, we use the DIFT score, GPTEval score, and CLIP score. The results are shown in Table 3 and Table 2. Our method shows the best CLIP score for text-to-3D semantic alignment. Regarding DIFT structural alignment, it yields strong results, albeit slightly lagging behind the exceptionally strong A3D and MVEdit scores. On GPTEval, it confidently beats MVEdit, while showing overall quality on par with A3D. The best quality of our method is its **speed**. It provides **x100** (!) speed-up compared with A3D and **x40** speed-up compared with MVEdit. The weaker side of our method is the lower score for *texture details* and *geometry details*. We observe this to be an inherent feature of the underlying Trellis backbone. Qualitative results are shown in the Figure 4, demonstrating the high degree of geometric alignment.

Figure 4. 3D Alignment Samples



5.3. Video

For video experiments, we modify the WAN 2.1 [51] rectified flow model according to our method. Due to the dynamic nature of video samples, unlike the static 3D objects and images, we compose a novel set of scenes for evaluation. We aim to cover diverse and complex scenarios, including animals in motion, cities, and human activities. We use two editing-based competitors, Lucy-edit [8] and VACE [21] (using depth-conditioned ControlNet). For editing-based models, we use WAN-generated videos as a source video. We also compare our setup with the joint generation method MatchDiffusion [38]. We observe that depth-conditioned VACE tends to preserve the general layout of the scene but significantly changes other aspects (poses, movements, objects, background, etc). On the other hand, Lucy-edit can produce precise manipulations but is observed to work well only for humans and some animals, making nonsensical edits for the majority of the examples. We present a quantitative comparison in Table 4. Our method demonstrates the highest DINO score, demonstrating the best self-consistency. While Lucy-edit formally shows lower depth MAE than our method, the reason for this is quite trivial - Lucy fails to provide necessary edits, leaving inputs intact. This is reflected by a very low VLM score for Lucy-edit, showing a disconnection between the videos and text descriptions. Despite the depth-conditioned setup, VACE exhibits the worst MAE alignment among all the methods, probably because of the distribution shift caused by the change of the prompt relative to the first image. On the other hand, MatchDiffusion shows good results both for VLM and DINO metrics but lags behind in terms of depth alignment, highlighting the need for a more principled approach. Depth absolute error for MatchDiffusion and our method is visualized in Figure 5. It is clearly seen that while for the background the difference in the depth is minimal for both methods, the contours of the foreground object are much more pronounced in the case of MatchD-

Table 4. Video Metrics.

	VLM \uparrow	DINO \uparrow	Depth MAE \downarrow
MatchDiffusion	<u>7,64</u>	0,96	1,12
Lucy-edit	4,77	0,97	0,84
VACE	6,26	<u>0,98</u>	2,60
Ours	7,66	0,98	0,89

Table 5. User study.

User study, % of comparisons where our method is preferred			
	Structural alignment	Video quality	Text-to-video consistency
vs. MatchDiffusion	67,50	58,60	47,00
vs. Lucy-edit	69,30	77,70	76,40
vs. VACE	88,00	60,90	58,60

iffusion, indicating the pose misalignment. We provide a user study Table 5 for the most revealing comparison. The user study demonstrates the superiority of our method over VACE and Lucy-edit in terms of the major criteria. The study also reinforces our hypothesis that our method provides superior structural alignment, showing a strong lead in this category over MatchDiffusion.

6. Ablation

To validate the design choices of our algorithm, we progressively remove the proposed components, simplifying the model step by step. After a series of such simplifications, our method effectively reduces to MatchDiffusion [38], allowing us to demonstrate—through a sequence of controlled comparisons the benefits of our approach.

We start from the setup (A), which is our full pipeline described in Section 4. Setup (B) is obtained by switch-



(a) Our method's source video frame (b) Our method's target video frame



(c) Depth difference between our method's source and target video frames



(d) MatchDiffusion's source video frame (e) MatchDiffusion's target video frame



(f) Depth difference between MatchDiffusion's source and target video frames

Figure 5. Visualization of geometry preservation between source and target video frames. Larger white areas means higher difference between corresponding pixels.

ing $v_t^{anchor} = \frac{v_t^a + v_t^b}{2}$ from $v_\Theta(\frac{x_t^a + x_t^b}{2}, t)$. Setup (C) degrades the pipeline further by avoiding sampling $x_{t,i}$ for the intermediate points. Without considering the intermediate points, the method does not optimize for the plausibility of the transitions between the samples, which is one of the core ideas of the method. When we move to setup (D), the only restriction synchronizing the movement of x_t^a and x_t^b left in place is the anchor velocity $v_t^{anchor} = \frac{v_t^a + v_t^b}{2}$. Instead of using the smooth schedule for weight coefficients,

		DIFT distance ↓ % of object size	
Depth MAE ↓		Setup A (ours)	6.44
Setup A (ours)	0.89	Setup A (ours)	6.44
Setup B	1.33	Setup D	8.42
Setup C	1.50	(b) DIFT distance ↓ (% of object size)	
	(a) Depth MAE ↓		

Table 6. Ablation study results. Lower is better (↓).



(a) Setup A (ours) (b) Setup B (c) Setup C (d) Setup D

Figure 6. Visualization of the impact of different components of our method. We can see that each component contributes to the results and that the results degrade as we gradually remove components from our algorithm.

we simplify it to a hard cutoff which makes the algorithm effectively equivalent to the MatchDiffusion [38] baseline. This step deprives the algorithm of a flexible co-guidance mechanism for the early stages of inference and removes any form of synchronization for the late stages. We evaluate setups (B) and (C) with the video pipeline reporting depth MAE structural score in Table 6a. Since the setup (D) is roughly equivalent to MatchDiffusion, for which we have already reported results in Section 5, we decide to evaluate this setup with the image modality; the results are shown in Table 6b. Visual examples for all the setups with the image pipeline are demonstrated in Figure 6. Quantitative and qualitative comparisons demonstrate a gradual degradation of the results during the component removal.

7. Conclusions

We present a new universal method for joint inference with rectified flow models, which enables the rapid production of structurally aligned samples across different modalities. Our method requires only a compact and local modification of the inference loop and can be applied on top of any pre-trained rectified flow model working with structured latent representations. We demonstrate the performance of our method across three modalities—video, 3D, and images — comparing it both with editing-based methods and joint training methods. Across all modalities, our method either achieves performance on par with the state of the art

or surpasses it. When applied to video modality, our method shows superior performance, enabling the accurate alignment of complex and vibrant environments. Our method has multiple potential applications, including the creation of aligned virtual environments and assets, and the generation of synthetic data. In future work, the method can be further applied to other modalities, such as 4D video and keypoint movements.

Acknowledgments

The work was supported by the grant for research centers in the field of AI provided by the Ministry of Economic Development of the Russian Federation in accordance with the agreement 000000C313925P4F0002 and the agreement with Skoltech №139-10-2025-033.

References

- [1] Omri Avrahami, Amir Hertz, Yael Vinker, Moab Arar, Shlomi Fruchter, Ohad Fried, Daniel Cohen-Or, and Dani Lischinski. The chosen one: Consistent characters in text-to-image diffusion models. *arXiv preprint arXiv:2311.10093*, 2023. [2](#), [3](#)
- [2] Elior Benarous, Yilun Du, and Heng Yang. Spie: Semantic and structural post-training of image editing diffusion models with ai feedback. In *Synthetic Data for Artificial Intelligence and Machine Learning: Tools, Techniques, and Applications III, Proceedings of SPIE Vol. 13459*, page 13459-0I (article ID) ??, 2025. [5](#)
- [3] David Berthelot*, Colin Raffel*, Aurko Roy, and Ian Goodfellow. Understanding and improving interpolation in autoencoders via an adversarial regularizer. In *International Conference on Learning Representations*, 2019. [3](#)
- [4] Black Forest Labs. FLUX.1 [dev]. <https://huggingface.co/black-forest-labs/FLUX.1-dev>, 2024. Open-weight rectified-flow text-to-image model. [2](#), [3](#), [5](#), [12](#)
- [5] Hansheng Chen, Ruoxi Shi, Yulin Liu, Bokui Shen, Jiayuan Gu, Gordon Wetzstein, Hao Su, and Leonidas J. Guibas. Generic 3d diffusion adapter using controlled multi-view editing. *arXiv preprint arXiv:2403.12032*, 2024. [2](#), [3](#), [5](#), [6](#)
- [6] Minghao Chen, Iro Laina, and Andrea Vedaldi. Dge: Direct gaussian 3d editing by consistent multi-view editing. In *European Conference on Computer Vision*, pages 74–92. Springer, 2024. [3](#)
- [7] Jaeyoung Chung, Suyoung Lee, Hyeongjin Nam, Jaerin Lee, and Kyoung Mu Lee. Luciddreamer: Domain-free generation of 3d gaussian splatting scenes. *arXiv preprint arXiv:2311.13384*, 2023. [3](#)
- [8] DecartAI Team. Lucy edit: Open-weight text-guided video editing, 2025. Technical report. [3](#), [7](#)
- [9] Patrick Esser, Sumith Kulal, Andreas Blattmann, Rahim Entezari, Jonas Müller, Harry Saini, Yam Levi, Dominik Lorenz, Axel Sauer, Frederic Boesel, et al. Scaling rectified flow transformers for high-resolution image synthesis. In *Forty-first international conference on machine learning*, 2024. [3](#)
- [10] Hyojun Go, Byeongjun Park, Jiho Jang, Jin-Young Kim, Soonwoo Kwon, and Changick Kim. Splatflow: Multi-view rectified flow model for 3d gaussian splatting synthesis. In *Proceedings of the Computer Vision and Pattern Recognition Conference*, pages 21524–21536, 2025. [3](#)
- [11] Ian Goodfellow, Jean Pouget-Abadie, Mehdi Mirza, Bing Xu, David Warde-Farley, Sherjil Ozair, Aaron Courville, and Yoshua Bengio. Generative adversarial networks. *Communications of the ACM*, 63(11):139–144, 2020. [3](#)
- [12] Google. Image editing in gemini just got a major upgrade, 2025. Describes *Nano Banana* (Gemini 2.5 Flash Image). Accessed: 2025-11-13. [2](#)
- [13] Amir Hertz, Andrey Voynov, Shlomi Fruchter, and Daniel Cohen-Or. Style aligned image generation via shared attention. In *Proceedings of the IEEE/CVF Conference on Computer Vision and Pattern Recognition (CVPR)*, pages 4775–4785, 2024. [2](#)
- [14] Jonathan Ho, Ajay Jain, and Pieter Abbeel. Denoising diffusion probabilistic models. *Advances in neural information processing systems*, 33:6840–6851, 2020. [3](#)
- [15] Wenyi Hong, Ming Ding, Wendi Zheng, Xinghan Liu, and Jie Tang. Cogvideo: Large-scale pretraining for text-to-video generation via transformers, 2022. [3](#)
- [16] Kaiyi Huang, Chengqi Duan, Kaiyue Sun, Enze Xie, Zhen-guo Li, and Xihui Liu. T2i-combench++: An enhanced and comprehensive benchmark for compositional text-to-image generation. *IEEE Transactions on Pattern Analysis and Machine Intelligence*, pages 1–17, 2025. [5](#)
- [17] Nick Huang, Aaron Gokaslan, Volodymyr Kuleshov, and James Tompkin. The gan is dead; long live the gan! a modern gan baseline. *Advances in Neural Information Processing Systems*, 37:44177–44215, 2024. [3](#)
- [18] Zehuan Huang, Yuan-Chen Guo, Haoran Wang, Ran Yi, Lizhuang Ma, Yan-Pei Cao, and Lu Sheng. Mv-adapter: Multi-view consistent image generation made easy. In *Proceedings of the IEEE/CVF International Conference on Computer Vision*, pages 16377–16387, 2025. [3](#)
- [19] Savva Victorovich Ignatyev, Nina Konovalova, Daniil Se-likhanovich, Oleg Voynov, Nikolay Patakin, Ilya Olkov, Dmitry Senushkin, Alexey Artemov, Anton Konushin, Alexander Filippov, Peter Wonka, and Evgeny Burnaev. A3d: Does diffusion dream about 3D alignment? In *International Conference on Learning Representations (ICLR)*, 2025. Poster. [2](#), [3](#), [5](#), [6](#), [12](#)
- [20] Zeyinzi Jiang, Zhen Han, Chaojie Mao, Jingfeng Zhang, Yulin Pan, and Yu Liu. Vace: All-in-one video creation and editing, 2025. [3](#)
- [21] Zeyinzi Jiang, Zhen Han, Chaojie Mao, Jingfeng Zhang, Yulin Pan, and Yu Liu. Vace: All-in-one video creation and editing. In *Proceedings of the IEEE/CVF International Conference on Computer Vision*, pages 17191–17202, 2025. [2](#), [5](#), [7](#)
- [22] Xuan Ju, Tianyu Wang, Yuqian Zhou, He Zhang, Qing Liu, Nanxuan Zhao, Zhifei Zhang, Yijun Li, Yuanhao Cai, Shaoteng Liu, Daniil Pakhomov, Zhe Lin, Soo Ye Kim, and

Qiang Xu. Editverse: Unifying image and video editing and generation with in-context learning, 2025. 5, 16

[23] Minguk Kang, Jun-Yan Zhu, Richard Zhang, Jaesik Park, Eli Shechtman, Sylvain Paris, and Taesung Park. Scaling up gans for text-to-image synthesis. In *Proceedings of the IEEE/CVF conference on computer vision and pattern recognition*, pages 10124–10134, 2023. 3

[24] Tero Karras, Samuli Laine, Miika Aittala, Janne Hellsten, Jaakko Lehtinen, and Timo Aila. Analyzing and improving the image quality of stylegan. In *2020 IEEE/CVF Conference on Computer Vision and Pattern Recognition (CVPR)*, pages 8107–8116, 2020. 3

[25] Diederik P Kingma and Max Welling. Auto-encoding variational bayes. *arXiv preprint arXiv:1312.6114*, 2013. 3

[26] Black Forest Labs, Stephen Batifol, Andreas Blattmann, Frederic Boesel, Saksham Consul, Cyril Diagne, Tim Dockhorn, Jack English, Zion English, Patrick Esser, et al. Flux. 1 kontext: Flow matching for in-context image generation and editing in latent space. *arXiv preprint arXiv:2506.15742*, 2025. 3

[27] Zeqiang Lai, Yunfei Zhao, Haolin Liu, Zibo Zhao, Qingxiang Lin, Huiwen Shi, Xianghui Yang, Mingxin Yang, Shuhui Yang, Yifei Feng, et al. Hunyuan3d 2.5: Towards high-fidelity 3d assets generation with ultimate details. *arXiv preprint arXiv:2506.16504*, 2025. 3

[28] Zeqiang Lai, Yunfei Zhao, Zibo Zhao, Haolin Liu, Fuyun Wang, Huiwen Shi, Xianghui Yang, Qingxiang Lin, Jingwei Huang, Yuhong Liu, et al. Unleashing vecset diffusion model for fast shape generation. *arXiv preprint arXiv:2503.16302*, 2025. 3

[29] Dong In Lee, Hyeongcheol Park, Jiyong Seo, Eunbyung Park, Hyunje Park, Ha Dam Baek, Sangheon Shin, Sangmin Kim, and Sangpil Kim. Editsplat: Multi-view fusion and attention-guided optimization for view-consistent 3d scene editing with 3d gaussian splatting. In *Proceedings of the Computer Vision and Pattern Recognition Conference*, pages 11135–11145, 2025. 3

[30] Yuseung Lee, Kunho Kim, Hyunjin Kim, and Minhyuk Sung. Syncdiffusion: Coherent montage via synchronized joint diffusions. *Advances in Neural Information Processing Systems*, 36:50648–50660, 2023. 3

[31] Jiahao Li, Hao Tan, Kai Zhang, Zexiang Xu, Fujun Luan, Yinghao Xu, Yicong Hong, Kalyan Sunkavalli, Greg Shakhnarovich, and Sai Bi. Instant3d: Fast text-to-3d with sparse-view generation and large reconstruction model. *arXiv preprint arXiv:2311.06214*, 2023. 3

[32] Lin Li, Zehuan Huang, Haoran Feng, Gengxiong Zhuang, Rui Chen, Chunchao Guo, and Lu Sheng. Voxhammer: Training-free precise and coherent 3d editing in native 3d space. *arXiv preprint arXiv:2508.19247*, 2025. 3

[33] Yuhan Li, Yishun Dou, Yue Shi, Yu Lei, Xuanhong Chen, Yi Zhang, Peng Zhou, and Bingbing Ni. Focaldreamer: Text-driven 3d editing via focal-fusion assembly. In *Proceedings of the AAAI conference on artificial intelligence*, pages 3279–3287, 2024. 3

[34] Yixun Liang, Xin Yang, Jiantao Lin, Haodong Li, Xiaogang Xu, and Yingcong Chen. Luciddreamer: Towards high-fidelity text-to-3d generation via interval score matching. *arXiv preprint arXiv:2311.11284*, 2023. 3, 6

[35] Xingchao Liu, Chengyue Gong, and Qiang Liu. Flow straight and fast: Learning to generate and transfer data with rectified flow. In *International Conference on Learning Representations (ICLR)*, 2023. 3

[36] Artem Lukoianov, Haitz Sáez de Ocáriz Borde, Kristjan Greenewald, Vitor Guizilini, Timur Bagautdinov, Vincent Sitzmann, and Justin M Solomon. Score distillation via reparametrized ddim. *Advances in Neural Information Processing Systems*, 37:26011–26044, 2024. 3

[37] Alejandro Pardo, Fabio Pizzati, Tong Zhang, Alexander Ponedaven, Philip Torr, Juan Camilo Perez, and Bernard Ghanem. Matchdiffusion: Training-free generation of match-cuts, 2024. 3

[38] Alejandro Pardo, Fabio Pizzati, Tong Zhang, Alexander Ponedaven, Philip Torr, Juan Camilo Perez, and Bernard Ghanem. Matchdiffusion: Training-free generation of match-cuts. In *Proceedings of the IEEE/CVF International Conference on Computer Vision (ICCV)*, 2025. 2, 3, 5, 7, 8

[39] William Peebles and Saining Xie. Scalable diffusion models with transformers. In *Proceedings of the IEEE/CVF international conference on computer vision*, pages 4195–4205, 2023. 3

[40] Ben Poole, Ajay Jain, Jonathan T Barron, and Ben Mildenhall. Dreamfusion: Text-to-3d using 2d diffusion. *arXiv preprint arXiv:2209.14988*, 2022. 3

[41] Qwen Team. Qwen-image-edit. <https://huggingface.co/Qwen/Qwen-Image-Edit>, 2025. Image editing foundation model based on Qwen-Image. 2, 3, 5

[42] Aditya Ramesh, Prafulla Dhariwal, Alex Nichol, Casey Chu, and Mark Chen. Hierarchical text-conditional image generation with clip latents. *arXiv preprint arXiv:2204.06125*, 1 (2):3, 2022. 3

[43] Tianhe Ren, Shilong Liu, Ailing Zeng, Jing Lin, Kun-chang Li, He Cao, Jiayu Chen, Xinyu Huang, Yukang Chen, Feng Yan, Zhaoyang Zeng, Hao Zhang, Feng Li, Jie Yang, Hongyang Li, Qing Jiang, and Lei Zhang. Grounded sam: Assembling open-world models for diverse visual tasks. *arXiv preprint arXiv:2401.14159*, 2024. 5

[44] Robin Rombach, Andreas Blattmann, Dominik Lorenz, Patrick Esser, and Björn Ommer. High-resolution image synthesis with latent diffusion models. In *Proceedings of the IEEE/CVF conference on computer vision and pattern recognition*, pages 10684–10695, 2022. 3

[45] Litu Rout, Yujia Chen, Nataniel Ruiz, Constantine Caramanis, Sanjay Shakkottai, and Wen-Sheng Chu. Semantic image inversion and editing using rectified stochastic differential equations. In *Proceedings of the Thirteenth International Conference on Learning Representations*, 2025. 3, 5

[46] Chitwan Saharia, William Chan, Saurabh Saxena, Lala Li, Jay Whang, Emily L Denton, Kamyar Ghasemipour, Raphael Gontijo Lopes, Burcu Karagol Ayan, Tim Salimans, et al. Photorealistic text-to-image diffusion models with deep language understanding. *Advances in neural information processing systems*, 35:36479–36494, 2022. 3

[47] Yichun Shi, Peng Wang, Jianglong Ye, Mai Long, Kejie Li, and Xiao Yang. Mvdream: Multi-view diffusion for 3d generation. *arXiv preprint arXiv:2308.16512*, 2023. 3

[48] Jiaming Song, Chenlin Meng, and Stefano Ermon. Denoising diffusion implicit models. *arXiv preprint arXiv:2010.02502*, 2020. 3

[49] Stanislaw Szymanowicz, Jason Y Zhang, Pratul Srinivasan, Ruiqi Gao, Arthur Brussee, Aleksander Holynski, Ricardo Martin-Brualla, Jonathan T Barron, and Philipp Henzler. Bolt3d: Generating 3d scenes in seconds. In *Proceedings of the IEEE/CVF International Conference on Computer Vision*, pages 24846–24857, 2025. 3

[50] Luming Tang, Menglin Jia, Qianqian Wang, Cheng Perng Phoo, and Bharath Hariharan. Emergent correspondence from image diffusion. In *Advances in Neural Information Processing Systems 36 (NeurIPS 2023)*, 2023. 5

[51] Team Wan, Ang Wang, Baole Ai, Bin Wen, Chaojie Mao, Chen-Wei Xie, Di Chen, Feiwu Yu, Haiming Zhao, Jianxiao Yang, et al. Wan: Open and advanced large-scale video generative models. *arXiv preprint arXiv:2503.20314*, 2025. 7

[52] Aaron Van Den Oord, Oriol Vinyals, et al. Neural discrete representation learning. *Advances in neural information processing systems*, 30, 2017. 3

[53] Team Wan, Ang Wang, Baole Ai, Bin Wen, Chaojie Mao, Chen-Wei Xie, Di Chen, Feiwu Yu, Haiming Zhao, Jianxiao Yang, Jianyuan Zeng, Jiayu Wang, Jingfeng Zhang, Jingren Zhou, Jinkai Wang, Jixuan Chen, Kai Zhu, Kang Zhao, Keyu Yan, Lianghua Huang, Mengyang Feng, Ningyi Zhang, Pandeng Li, Pingyu Wu, Ruihang Chu, Ruili Feng, Shiwei Zhang, Siyang Sun, Tao Fang, Tianxing Wang, Tianyi Gui, Tingyu Weng, Tong Shen, Wei Lin, Wei Wang, Wei Wang, Wenmeng Zhou, Wente Wang, Wenting Shen, Wenyuan Yu, Xianzhong Shi, Xiaoming Huang, Xin Xu, Yan Kou, Yangyu Lv, Yifei Li, Yijing Liu, Yiming Wang, Yingya Zhang, Yitong Huang, Yong Li, You Wu, Yu Liu, Yulin Pan, Yun Zheng, Yuntao Hong, Yupeng Shi, Yutong Feng, Zeyinzi Jiang, Zhen Han, Zhi-Fan Wu, and Ziyu Liu. Wan: Open and advanced large-scale video generative models, 2025. 3

[54] Chenfei Wu, Jiahao Li, Jingren Zhou, Junyang Lin, Kaiyuan Gao, Kun Yan, Sheng ming Yin, Shuai Bai, Xiao Xu, Yilei Chen, Yuxiang Chen, Zecheng Tang, Zekai Zhang, Zhengyi Wang, An Yang, Bowen Yu, Chen Cheng, Dayiheng Liu, Deqing Li, Hang Zhang, Hao Meng, Wei Hu, Jingyuan Ni, Kai Chen, Kuan Cao, Liang Peng, Lin Qu, Minggang Wu, Peng Wang, Shuting Yu, Tingkun Wen, Wensen Feng, Xiaoxiao Xu, Yi Wang, Yichang Zhang, Yongqiang Zhu, Yujia Wu, Yuxuan Cai, and Zenan Liu. Qwen-image technical report, 2025. 2, 3, 5

[55] Guanjun Wu, Jiemin Fang, Chen Yang, Sikuang Li, Taoran Yi, Jia Lu, Zanwei Zhou, Jiazhong Cen, Lingxi Xie, Xiaopeng Zhang, et al. Unilat3d: Geometry-appearance unified latents for single-stage 3d generation. *arXiv preprint arXiv:2509.25079*, 2025. 3

[56] Tong Wu, Guandao Yang, Zhibing Li, Kai Zhang, Ziwei Liu, Leonidas J. Guibas, Dahua Lin, and Gordon Wetzstein. GPT-4V(ision) is a Human-Aligned Evaluator for Text-to-3D Generation. In *Proceedings of the IEEE/CVF Conference on Computer Vision and Pattern Recognition (CVPR)*, 2024. 5

[57] Jianfeng Xiang, Zelong Lv, Sicheng Xu, Yu Deng, Ruicheng Wang, Bowen Zhang, Dong Chen, Xin Tong, and Jiaolong Yang. Structured 3d latents for scalable and versatile 3d generation. *arXiv preprint arXiv:2412.01506*, 2024. 3, 6

[58] Lihe Yang, Bingyi Kang, Zilong Huang, Zhen Zhao, Xiaogang Xu, Jiaoshi Feng, and Hengshuang Zhao. Depth anything v2. *arXiv:2406.09414*, 2024. 5, 16

[59] Yuanbo Yang, Jiahao Shao, Xinyang Li, Yujun Shen, Andreas Geiger, and Yiyi Liao. Prometheus: 3d-aware latent diffusion models for feed-forward text-to-3d scene generation. In *Proceedings of the Computer Vision and Pattern Recognition Conference*, pages 2857–2869, 2025. 3

[60] Junliang Ye, Shenghao Xie, Ruowen Zhao, Zhengyi Wang, Hongyu Yan, Wenqiang Zu, Lei Ma, and Jun Zhu. Nano3d: A training-free approach for efficient 3d editing without masks. *arXiv preprint arXiv:2510.15019*, 2025. 3

[61] Kyeongmin Yeo, Jaihoon Kim, and Minhyuk Sung. Stochsync: Stochastic diffusion synchronization for image generation in arbitrary spaces. *arXiv preprint arXiv:2501.15445*, 2025. 3

[62] Zibo Zhao, Zeqiang Lai, Qingxiang Lin, Yunfei Zhao, Haolin Liu, Shuhui Yang, Yifei Feng, Mingxin Yang, Sheng Zhang, Xianghui Yang, et al. Hunyuan3d 2.0: Scaling diffusion models for high resolution textured 3d assets generation. *arXiv preprint arXiv:2501.12202*, 2025. 3

[63] Jingyu Zhuang, Chen Wang, Liang Lin, Lingjie Liu, and Guanbin Li. Dreameditor: Text-driven 3d scene editing with neural fields. In *SIGGRAPH Asia 2023 Conference Papers*, pages 1–10, 2023. 3

[64] Jingyu Zhuang, Di Kang, Yan-Pei Cao, Guanbin Li, Liang Lin, and Ying Shan. Tip-editor: An accurate 3d editor following both text-prompts and image-prompts. *ACM Transactions on Graphics (TOG)*, 43(4):1–12, 2024. 3

ATATA: One Algorithm to Align Them All

Supplementary Material

A. Competitor details

A.1. 2D competitors

For running competitors, we use the same pair of text prompts. Source prompt corresponds to the first prompt in the pair, and the target prompt corresponds to the second prompt in the pair.

1. **Qwen-Image-Edit.** We use the most recent release of the model from 25.09. The source image is generated by FLUX [4] using the source prompt. For target image generation, we modify the prompt from 'target prompt' to "change 'source prompt' to 'target prompt', preserving geometry and background"
2. **Rf-inversion.** We generate the source image with the FLUX model [4]. Hyperparameters for target generation are $t_{stop} = 6/28$, $\eta = 0.9$, $n_{steps} = 28$.

A.2. 3D competitors

For 3D evaluation, we use the 3D models, renders, and numerical results from A3D paper [19].

A.3. Video competitors

1. **LucyEdit.** We use a WAN model to generate source videos. We edit them using 2 keywords: 'replace' - for changing the main character on the scene, and 'transform' - for performing global scene-level edits.
2. **VACE.** We use WAN to generate source videos. We edit them using Wan2.1-VACE-1.3B, conditioned on source video depth.
3. **MatchDiffusion** We use exactly the same prompts as for the main method, which are presented in the Table 11.

B. Math details

B.1. Integral form

In Section 4.1, we have derived the formulas for the single-step update for our method. While these formulas are analytically correct, the update depends on the placement and the number of the sampled points, and not only on the distribution $p(\alpha)$. If we set $\lim_{k \rightarrow \infty}$ in Equation 3, we obtain the formulas in the integral form (omitting

$$\mathcal{L}(x_{t_2}^a, x_{t_2}^b) = \int_0^1 p(\alpha) \|x_{t_2}(\alpha) - \hat{x}_{t_2}(\alpha)\|^2 d\alpha, \quad (10)$$

$$\hat{x}_{t_2}(\alpha) = x_{t_1}(\alpha) + (t_2 - t_1) v_\Theta(x_{t_1}(\alpha), t_1, c(\alpha))$$

$$x_{t_2}(\alpha) = (1 - \alpha) x_{t_2}^a + \alpha x_{t_2}^b$$

$$x_{t_1}(\alpha) = (1 - \alpha) x_{t_1}^a + \alpha x_{t_1}^b$$

We can also rewrite $\hat{x}_{t_2}(\alpha)$ in the differential form:

$$\hat{x}_{t_2}(\alpha) = x_{t_1}(\alpha) + dt v_\Theta(x_{t_1}(\alpha), t_1, c(\alpha)) \quad (11)$$

We can also rewrite the solution of the regression within the same logic.

$$\begin{aligned} c_{00} &= \int_{\alpha=0}^1 p(\alpha)(1-\alpha)^2 d\alpha, & c_{01} &= \int_{\alpha=0}^1 p(\alpha)(1-\alpha)\alpha d\alpha, \\ c_{11} &= \int_{\alpha=0}^1 p(\alpha)\alpha^2 d\alpha, & \Delta &= c_{00}c_{11} - c_{01}^2, \\ d_0 &= \int_{\alpha=0}^1 p(\alpha)(1-\alpha)\hat{x}_{t_2}(\alpha) d\alpha, & d_1 &= \int_{\alpha=0}^1 p(\alpha)\alpha \hat{x}_{t_2}(\alpha) d\alpha, \end{aligned}$$

We can use Equation 11 to write out:

$$\begin{aligned} d_0 &= \int_{\alpha=0}^1 p(\alpha)(1 - \alpha)x_{t_1}(\alpha) d\alpha + \\ &\quad dt \int_{\alpha=0}^1 p(\alpha)(1 - \alpha)v_\Theta(x_{t_1}(\alpha), t_1, c(\alpha)) d\alpha, \\ d_1 &= \int_{\alpha=0}^1 p(\alpha) \alpha x_{t_1}(\alpha) d\alpha + \\ &\quad dt \int_{\alpha=0}^1 p(\alpha) \alpha v_\Theta(x_{t_1}(\alpha), t_1, c(\alpha)) d\alpha \end{aligned} \quad (12)$$

Here we split the integral into the sum of two integrals, where only the second integral is dependent on velocity and dt . Using

$$x_{t_2}^a = \frac{c_{11}d_0 - c_{01}d_1}{\Delta}, \quad x_{t_2}^b = \frac{c_{00}d_1 - c_{01}d_0}{\Delta}, \quad (13)$$

After simplification, we derive:

$$\begin{aligned} x_{t_1+dt}^a &= x_{t_1}^a + \frac{dt}{\Delta} (c_{11}\mu_0 - c_{01}\mu_1) \\ x_{t_1+dt}^b &= x_{t_1}^b + \frac{dt}{\Delta} (c_{00}\mu_1 - c_{01}\mu_0) \\ \mu_0 &= \int_0^1 p(\alpha)(1 - \alpha)v_\Theta(x_{t_1}(\alpha), t_1, c(\alpha)) d\alpha \\ \mu_1 &= \int_0^1 p(\alpha)\alpha v_\Theta(x_{t_1}(\alpha), t_1, c(\alpha)) d\alpha \end{aligned} \quad (14)$$

Now we can write out $v_{t_1}^a$ and $v_{t_1}^b$. It can be seen that it only depends on the velocity-weighted closed integral.

$$v_{t_1}^a = \frac{c_{11}\mu_0 - c_{01}\mu_1}{\Delta} \quad v_{t_1}^b = \frac{c_{00}\mu_1 - c_{01}\mu_0}{\Delta} \quad (15)$$

We have derived the precise continuous version for the conversion of the rectified flow into the velocity field for segments. Note that we can use different approximations to calculate the integrals for μ_0 and μ_1 , not necessarily using an even grid. For example, we can employ the Monte-Carlo method using the probability $p(\alpha)$ to sample points randomly from $\alpha \in [0, 1]$.

B.2. Probability matching

We can show that under certain restrictions, our algorithm can be seen as conserving the probability distribution of the points moving along the v_θ trajectories. Our primary goal is to conserve the probability distribution $p(\alpha)$.

We define the target and approximate noisy marginals as

$$p_t^{\text{true}}(x) = \int_0^1 p(\alpha) \mathcal{N}(x | x_t^{\text{true}}(\alpha), \sigma^2 I) d\alpha, \quad (16)$$

$$p_t^{\text{approx}}(x) = \int_0^1 p(\alpha) \mathcal{N}(x | x_t^{\text{approx}}(\alpha), \sigma^2 I) d\alpha. \quad (17)$$

It is convenient to consider the joint distributions over (x, α) :

$$p_t^{\text{true}}(x, \alpha) = p(\alpha) \mathcal{N}(x | x_t^{\text{true}}(\alpha), \sigma^2 I), \quad (18)$$

$$p_t^{\text{approx}}(x, \alpha) = p(\alpha) \mathcal{N}(x | x_t^{\text{approx}}(\alpha), \sigma^2 I). \quad (19)$$

For fixed α , both conditionals $p_t^{\text{true}}(x | \alpha)$ and $p_t^{\text{approx}}(x | \alpha)$ are Gaussians with the same covariance $\sigma^2 I$, so their conditional KL divergence is

$$\text{KL}(p_t^{\text{true}}(x | \alpha) \| p_t^{\text{approx}}(x | \alpha)) = \quad (20)$$

$$= \frac{1}{2\sigma^2} \|x_t^{\text{true}}(\alpha) - x_t^{\text{approx}}(\alpha)\|^2. \quad (21)$$

Taking the expectation with respect to $p(\alpha)$ yields the joint KL

$$\text{KL}(p_t^{\text{true}}(x, \alpha) \| p_t^{\text{approx}}(x, \alpha)) = \quad (22)$$

$$= \frac{1}{2\sigma^2} \mathbb{E}_{\alpha \sim p} \|x_t^{\text{true}}(\alpha) - x_t^{\text{approx}}(\alpha)\|^2.$$

As $\sigma \rightarrow 0$, the KL divergence between the marginals $p_t^{\text{true}}(x)$ and $p_t^{\text{approx}}(x)$ differs from the joint KL only by an $\mathcal{O}(1)$ term, so we obtain the asymptotic

$$\text{KL}(p_t^{\text{true}} \| p_t^{\text{approx}}) = \quad (23)$$

$$= \frac{1}{2\sigma^2} \mathbb{E}_{\alpha \sim p} \|x_t^{\text{true}}(\alpha) - x_t^{\text{approx}}(\alpha)\|^2 + \mathcal{O}(1), \quad \sigma \rightarrow 0.$$

Thus, minimizing the L^2 objective

$$\mathbb{E}_{\alpha \sim p} \|x_t^{\text{true}}(\alpha) - x_t^{\text{approx}}(\alpha)\|^2, \quad (24)$$

Eq. 23, is equivalent to minimizing $\text{KL}(p_t^{\text{true}} \| p_t^{\text{approx}})$ at leading order in σ^{-2} .

B.3. Plausibility optimization

Our segment-based rectified flow formulation can be interpreted as optimizing the log-likelihood of all samples along the segment, not just its endpoints. This perspective connects our approach to the fundamental likelihood maximization principle in continuous normalizing flows.

We have shown that for small σ , $p_{t_2}^{\text{true}}(x)$ concentrates around the true trajectory $\hat{x}_{t_2}(\alpha)$. Thus, minimizing \mathcal{L} directly maximizes the expected log-likelihood of all points along our segment under the true data distribution.

Any sample drawn from a point along the segment (according to $p(\alpha)$) will have high likelihood under the target distribution, preserving the core property of rectified flows while maintaining the geometric structure of segments.

C. User study details

In the user study, annotators were asked to evaluate generated video pairs based on three criteria:

- 1. Alignment.** *In which row are Video A and Video B better aligned with each other in terms of overall structure, overall meaning, pose, and 3D geometry?*
- 2. Visual Appeal.** *In which row is the pair Video A and Video B more visually appealing in terms of realism, smoothness, and overall perceptual quality?*
- 3. Text Prompt Consistency.** *In which row do Video A and Video B better match their textual description?*

Figure 7 shows an example task from the study. All videos in the task were played simultaneously for the annotator with the ability to view them frame-by-frame.

For each question, annotators could choose between three options: preference for the first row, preference for the second row, or no preference.

We generated examples for the User Study using 21 pairs from a diverse set of scenes described in Table 11. To reduce bias, the rows were randomly swapped. At least seven different individuals annotated each task, and their responses were aggregated for analysis, resulting in a total of 2379 answers from 60 unique users across 63 tasks.

D. Full ablation

We provide the detailed ablation experiments with image modality in Table 7. We also provide the version of the setup (D) without finding the best-performing hyperparameter (the number of joint steps), which is obtained directly by removing the component from the setup (C). In this way, we show that the removal of the essential components leads to consistent degradation of the essential metrics. The only exception is the improvement observed when moving from setup (C) to setup (D). Sampling intermediate points $x_{t,i}$ and setting $v_t^{\text{anchor}} = v_\theta(\frac{x_t^a + x_t^a}{2})$ are strongly interconnected and were both proposed together for joint segment

Description for **Video A:**

^A
running dog-animal sprinting along a dirt path in the park under the morning light

1

Description for **Video B:**

^A
running dog-robot sprinting along a dirt path in the park under the morning light

2



Figure 7. User study image example.

transport. Consequently, using only intermediate points sampling alone can be less effective and even detrimental. Our primary aim here is not to optimize each intermediate variant, but to demonstrate that the endpoint of this sequential component removal—corresponding to the MatchDiffusion setup—exhibits degraded performance compared to our full method.

E. Additional image generation results

Additional examples of applying our method to aligned image generation are presented in 8.

F. Metrics details

We primarily address the question of whether alignment can be achieved between the source image and the generated target image when the source prompt is modified into the target prompt. This process is evaluated based on two main

criteria: 1) whether the generated target image accurately corresponds to the target prompt, and 2) whether proper alignment is maintained between the source image and the generated target image.

F.1. 2D Metrics

For 2D images, we employ the DIFT metric to evaluate the similarity between two images.

$$S_{DIFT} = \frac{1}{2N} \sum_{i=1}^N \frac{\|F_A(P_i^A) - P_i^A\|_2}{\sigma_{P_A}} + \frac{\|F_B(P_i^B) - P_i^B\|_2}{\sigma_{P_B}},$$

By uniformly sampling the masked image, we extract a dense point cloud of the object, which is then used to locate the most corresponding target point cloud in the aligned image. The alignment between the two images is assessed by computing the L2 distance between corresponding points in the two point clouds. To account for the influence of the object scale on distance calculation, we normalize the

Table 7. Full Ablation.

Scene	DIIT w thres ↓					Depth L1 ↓					CLIP ↑					MLM-based score ↑				
	Ablation A	Ablation B	Ablation C	Ablation D	Ablation D untuned	Ablation A	Ablation B	Ablation C	Ablation D	Ablation D untuned	Ablation A	Ablation B	Ablation C	Ablation D	Ablation D untuned	Ablation A	Ablation B	Ablation C	Ablation D	Ablation D untuned
ant	11,2	15,7	15,5	12,6	16,2	36,9	47,7	52,8	42,3	48,6	26,9	28,2	28,4	28,3	28,2	94,0	100,0	99,0	98,0	100,0
bike	2,5	7,5	12,8	3,1	7,4	12,8	33,7	48,9	46,4	34,9	18,6	19,5	20,0	20,0	19,5	64,0	75,0	99,0	77,0	76,0
bird_dino	9,2	14,6	14,0	12,9	14,8	38,6	52,1	58,6	49,9	50,1	24,8	23,8	24,5	23,9	23,8	92,0	100,0	100,0	100,0	99,0
car	0,6	17,9	17,5	8,7	11,6	3,9	59,9	92,2	39,9	51,9	17,5	20,6	21,8	19,7	20,2	60,0	91,0	98,0	76,0	82,0
dwarf_minotaur	7,2	9,2	12,8	11,1	9,9	36,9	44,0	57,3	41,6	48,1	25,7	26,0	25,3	25,3	25,0	81,0	82,0	75,0	82,0	76,0
gopher	3,3	7,8	8,9	3,9	8,7	15,3	28,2	35,4	16,8	33,2	24,1	24,7	25,7	24,4	25,8	77,0	77,0	84,0	66,0	83,0
horse_skeleton	5,2	11,0	13,5	5,6	8,4	34,5	72,1	92,2	34,0	58,8	27,3	27,1	27,1	26,5	25,9	86,0	93,0	97,0	84,0	83,0
lego	4,6	4,9	9,7	3,0	6,0	23,5	23,2	41,0	20,2	31,0	22,3	23,0	22,6	21,7	21,8	93,0	94,0	94,0	87,0	86,0
magnolia	4,0	6,0	11,1	4,6	9,5	25,7	50,7	57,4	28,8	49,2	25,3	24,4	25,8	24,0	25,1	94,0	93,0	98,0	87,0	91,0
marine_gen2	8,0	12,6	12,8	11,6	10,9	44,4	64,1	69,4	54,0	47,1	21,7	22,3	23,1	23,3	22,7	69,0	83,0	86,0	80,0	79,0
mermaid	11,4	13,5	15,2	12,5	15,3	39,6	41,6	48,1	39,8	47,1	26,8	26,8	27,0	27,1	27,2	94,0	97,0	100,0	100,0	100,0
robot_gen2	5,4	13,2	13,8	6,5	10,2	27,2	83,2	80,3	41,5	50,9	18,5	20,7	21,3	19,5	20,0	84,0	84,0	92,0	75,0	83,0
ship	8,7	18,2	20,6	11,0	12,7	13,0	28,8	30,8	16,8	20,6	21,0	22,3	22,3	21,3	21,7	66,0	73,0	73,0	65,0	67,0
temple	10,5	9,9	14,5	10,5	14,1	27,2	42,2	39,6	41,2	32,1	24,2	23,3	24,9	23,6	24,1	91,0	91,0	99,0	100,0	98,0
throne	4,9	11,6	15,2	4,8	13,0	23,0	55,2	67,4	24,2	40,9	24,1	24,3	23,8	22,5	24,5	96,0	100,0	98,0	88,0	99,0
Avg	6,4	11,6	13,8	8,2	11,3	26,8	48,4	58,1	35,8	43,0	23,2	23,8	24,2	23,4	23,7	83,3	88,8	92,8	84,3	86,8



(a) A zebra is drinking vs A tiger is drinking



(b) Comb jelly undulating in bioluminescent threads vs 'larval octopus undulating in bioluminescent threads, pigeons startled'



(c) Concert stage with a pianist and a cellist performing in counterpoint vs Concert stage with a harpist and a flutist performing in counterpoint



(d) Farm lane with two tractors rolling past hay bales vs Farm lane with two horses pulling wagons past hay bales



(e) Limestone cave chamber vs Glacial ice cave chamber



(f) Open steppe with a sweeping herd of antelope crossing a river braid vs Open steppe with a sweeping herd of wild horses crossing a river braid



(g) Rainy gutter stream with paper boats drifting past curb leaves vs Rainy gutter stream with wooden toy boats drifting past curb leaves



(h) Art tabletop with ink plumes blooming in a paper marbling bath vs Art tabletop with paint plumes blooming in a paper marbling bath



(i) Tundra thermals with a snowy owl hovering above frost grass vs Tundra thermals with a frost wyvern hovering above frost grass

Figure 8. Aligned image generation results

point clouds based on the size of the object. Additionally, to mitigate the impact of outlier points on the overall point cloud distance calculation, a distance threshold of 50 pixels is applied. To evaluate text-image alignment, we initially consider using the CLIP score as a metric. However, due to its limited interpretability, we adopt the evaluation approach from T2I-CompBench++, which employs the GPT-4o model to assess the alignment between text and images. This method, based on a multimodal large language model, not only provides a score but also offers textual explanations justifying the rating. To better highlight performance differences across methods, we uniformly scale up the original scores. We provide full results for different scenes in Table 8, our method demonstrates superior image alignment compared to Qwen and RF-Inversion. Although it slightly underperforms in text-image consistency, the difference is visually negligible.

F.2. 3D Metrics

Analogous to the evaluation of 2D images, we also assess 3D objects using the DIFT metric. The key distinction lies in our preliminary step of rendering each 3D object from 120 different viewpoints, resulting in 120 corresponding 2D images. The DIFT metric is then computed using the images rendered from both the source and target 3D objects. To evaluate text-image alignment, we compute the CLIP score using the rendered 2D images. As shown in Table 9, with full results split into different scenes our method achieves competitive but slightly lower image alignment compared to A3D and MVEdit, while significantly outperforming LucidDreamer. In addition, the GPTEval3D metric was employed to assess performance across six dimensions: text-asset alignment, 3D plausibility, text-geometry alignment, texture Details, geometry details, and overall.

F.3. Video Metrics

The goal of video generation metrics is to evaluate all aspects of video pair generation: not only how well the geometry of the scene is preserved, but also how well the resulting videos look, their similarity to the prompt, etc. We use 3 metrics in total, which cover all the requirements we want from video generation:

1. **VLM evaluation.** We ask multi-modal LLM(gpt-4o) to give scores to 3 aspects: prompt following, edit quality, and background consistency. Every aspect might give 3 points in total. [22]
2. **DiNO consistency.** We evaluate the temporal consistency of the whole video by calculating the cosine similarity between DiNO features of the consecutive frames. Instead of considering all DiNO features, we compare only 'cls' tokens, which accumulate the overall semantics of the frames. [22]
3. **Depth difference.** When generating pairs of videos, we

want the geometry of the scene within pairs to be as close as possible as the reflection of the scene structure. We use the DepthAnything2 [58] model to estimate per-pixel depth and then calculate the difference between the depths of the corresponding pixels on the source and target videos.

We present the full results for all the scenes in the Table 10.

G. Experiment details

Our method depends on several schedules described in the Method section, such as the schedule of consistency scales w_t in smoothness regularization and the schedule of $p(\alpha_i)$. We found that sampling only four α points is sufficient for approximation of the integral in Equation 14 to obtain plausible transitions between two objects in all three modalities. We also found that the best scheduling for w_t is a piecewise constant non-increasing function with several discontinuities that reduces the effect of regularization as the denoising timestep increases. This holds for all modalities.

G.1. Generating aligned images

We use the following w_t schedule and $p(\alpha)$ density in our image generation experiments.

$$w_t = \begin{cases} 0.7 & \text{if } t < 7 \\ 0.5 & \text{if } t = 7 \\ 0.4 & \text{if } t = 8 \\ 0.1 & \text{if } t > 8 \end{cases}$$

$$p(\alpha) \propto \begin{cases} p_{\mathcal{U}[0,0.1]}(\alpha) & \text{if } \alpha \in [0, 0.1) \\ 0 & \text{if } \alpha \in [0.1, 0.3) \\ 0.87 p_{\mathcal{U}[0.3,0.5]}(\alpha) & \text{if } \alpha \in [0.3, 0.5) \\ 0.5 & \text{if } \alpha = 0.5 \\ 0.87 p_{\mathcal{U}(0.5,0.7)}(\alpha) & \text{if } \alpha \in (0.5, 0.7) \\ 0 & \text{if } \alpha \in [0.7, 0.9) \\ p_{\mathcal{U}[0.9,1]}(\alpha) & \text{if } \alpha \in [0.9, 1.0], \end{cases}$$

G.2. Generating aligned videos

We use the following w_t schedule and $p(\alpha)$ density in our video generation experiments.

$$w_t = \begin{cases} 0.5 & \text{if } t < 7 \\ 0.4 & \text{if } t = 7 \\ 0.3 & \text{if } t = 8 \\ 0.1 & \text{if } t > 8 \end{cases}$$

Table 8. 2D Metrics.

Scene	DIFT w thres ↓			Depth L1 ↓			CLIP ↑			MLLM-based score ↑		
	Qwen	RF_Inversion	Ours	Qwen	RF_Inversion	Ours	Qwen	RF_Inversion	Ours	Qwen	RF_Inversion	Ours
ant	17,7	16,6	11,2	33,3	25,5	36,9	26,7	26,9	26,9	96,0	96,0	94,0
bike	14,1	4,0	2,5	42,4	30,3	12,8	22,2	21,1	18,6	100,0	66,0	64,0
bird_dino	13,5	10,3	9,2	46,6	25,3	38,6	23,7	23,9	24,8	100,0	92,0	92,0
car	14,1	3,2	0,6	46,7	13,8	3,9	22,8	17,3	17,5	94,0	60,0	60,0
dwarf_minotaur	10,9	9,2	7,2	47,7	37,5	36,9	26,5	26,1	25,7	90,0	84,0	81,0
gopher	14,4	10,7	3,3	29,4	25,9	15,3	25,8	25,9	24,1	90,0	92,0	77,0
horse_skeleton	10,6	3,8	5,2	69,9	20,1	34,5	27,0	24,2	27,3	92,0	64,0	86,0
lego	7,4	3,5	4,6	28,1	24,2	23,5	25,3	22,6	22,3	98,0	78,0	93,0
magnolia	8,3	6,4	4,0	58,8	47,2	25,7	25,5	23,8	25,3	100,0	92,0	94,0
marine_gen2	6,9	7,1	8,0	29,3	40,3	44,4	21,6	24,7	21,7	66,0	82,0	69,0
mermaid	5,1	14,2	11,4	20,3	44,4	39,6	25,0	25,9	26,8	84,0	94,0	94,0
robot_gen2	12,9	6,3	5,4	40,4	34,1	27,2	22,9	19,6	18,5	100,0	84,0	84,0
ship	13,7	14,1	8,7	9,0	19,5	13,0	22,0	21,9	21,0	74,0	76,0	66,0
temple	4,1	8,6	10,5	16,1	23,7	27,2	20,2	24,5	24,2	60,0	100,0	91,0
throne	16,3	11,5	4,9	46,7	15,9	23,0	24,6	22,2	24,1	100,0	86,0	96,0
Avg	11,3	8,6	6,4	37,6	28,5	26,8	24,1	23,4	23,2	89,6	83,1	83,3

Table 9. 3D Metrics.

Scene	DIFT w thres ↓				CLIP ↑			
	A3D	MVEdit	LucidDreamer	Ours	A3D	MVEdit	LucidDreamer	Ours
ant	5,0	5,0	10,7	8,7	28,0	29,2	24,8	28,5
bike	4,9	4,5	7,0	5,1	25,7	26,7	26,2	26,3
bird_dino	7,0	6,4	15,7	14,5	26,8	24,0	25,0	26,0
car	4,0	3,0	10,5	8,3	29,1	21,8	28,9	29,5
dwarf_minotaur	5,2	6,0	9,3	4,9	26,8	27,2	24,4	31,1
gopher	4,7	5,9	10,2	3,3	28,6	25,0	25,6	29,1
horse_skeleton	6,7	2,1	4,2	7,5	29,1	26,7	24,4	31,2
lego	5,3	5,1	16,7	6,5	24,3	25,9	25,4	27,4
magnolia	2,3	9,0	14,3	5,5	30,6	30,2	24,3	25,1
marine_gen2	7,0	3,2	13,7	3,3	25,2	28,4	24,6	27,1
mermaid	7,3	10,4	14,3	13,3	29,9	30,4	27,6	30,1
robot_gen2	5,8	3,4	11,7	2,3	29,9	30,7	26,8	30,8
ship	15,7	9,7	8,7	7,0	28,2	27,1	27,8	26,7
temple	3,7	4,9	12,2	4,4	26,7	26,6	31,3	25,8
throne	2,6	3,2	10,1	10,1	26,7	26,6	28,9	29,8
Avg	5,8	5,5	11,3	7,0	27,7	27,1	26,4	28,3

$$p(\alpha) \propto \begin{cases} p_{U[0,0.1]}(\alpha) & \text{if } \alpha \in [0, 0.1) \\ 0 & \text{if } \alpha \in [0.1, 0.3) \\ 0.25 p_{U[0.3,0.5]}(\alpha) & \text{if } \alpha \in [0.3, 0.5) \\ 0.15 & \text{if } \alpha = 0.5 \\ 0.25 p_{U(0.5,0.7)}(\alpha) & \text{if } \alpha \in (0.5, 0.7) \\ 0 & \text{if } \alpha \in [0.7, 0.9) \\ p_{U[0.9,1]}(\alpha) & \text{if } \alpha \in [0.9, 1.0], \end{cases}$$

G.3. Generating aligned 3D objects

We use the Trellis model as the backbone text-to-3D Flow Matching model. This model consists of two main parts. The first Flow Matching model is used to densely denoise and obtain a structured latent - sparse geometry representation. When the geometry is fixed, the second model is used

to denoise the structured latents to obtain the details for the earlier estimated geometry. As we are interested in aligning geometry only, we incorporated our method only in the dense denoising part.

We use the following w_t schedule and $p(\alpha)$ density in our 3D generation experiments. In this way, the approximation of the 14 can be achieved by sampling single points from the probability regions with non-zero density $p(\alpha)$ with the corresponding summarized probabilities.

$$w_t = \begin{cases} 0.7 & \text{if } t < 12 \\ 0.05 & \text{if } t > 12 \end{cases}$$

$$p(\alpha) \propto \begin{cases} p_{\mathcal{U}[0,0.1]}(\alpha) & \text{if } \alpha \in [0, 0.1) \\ 0 & \text{if } \alpha \in [0.1, 0.3) \\ 0.35 p_{\mathcal{U}[0.3,0.5]}(\alpha) & \text{if } \alpha \in [0.3, 0.5) \\ 0.5 & \text{if } \alpha = 0.5 \\ 0.35 p_{\mathcal{U}(0.5,0.7)}(\alpha) & \text{if } \alpha \in (0.5, 0.7) \\ 0 & \text{if } \alpha \in [0.7, 0.9) \\ p_{\mathcal{U}[0.9,1]}(\alpha) & \text{if } \alpha \in [0.9, 1.0], \end{cases}$$

G.4. Prompts

For video and 3D experiments, we have to use the detailed versions on the prompts, since modern models tend to perform much better with long and detailed prompts than with short ones. We provide the full prompts for 3D experiments in Table 12 and full prompts for video experiments in Table 11.

Table 10. Video Metrics.

Scene	DINO \uparrow				Depth MAE \downarrow				VLM \uparrow			
	MatchDiffusion	Lucy-edit	VACE	Ours	MatchDiffusion	Lucy-edit	VACE	Ours	MatchDiffusion	Lucy-edit	VACE	Ours
apartment	0,99	1,00	1,00	1,00	1,02	0,19	1,58	0,45	8,00	3,33	9,00	9,00
blacksmith	0,95	0,99	1,00	0,99	0,79	0,82	4,08	1,22	9,00	5,00	5,33	4,50
car_carriage	0,98	0,97	0,96	1,00	2,88	1,15	2,44	1,14	8,25	4,00	6,00	6,50
chimney	0,99	1,00	0,99	1,00	0,26	0,62	4,81	0,93	8,00	4,00	7,67	7,25
city	0,99	0,99	1,00	0,99	0,89	0,67	4,25	1,07	8,75	7,00	7,00	9,00
climbing	0,98	0,99	0,99	1,00	1,92	0,60	3,64	1,23	7,00	3,00	7,33	7,00
cooking	1,00	1,00	0,99	1,00	1,11	1,11	3,58	1,11	6,75	4,00	6,00	8,00
desert	0,99	0,94	0,99	1,00	0,35	0,87	0,22	0,57	3,00	4,33	5,00	6,00
dino_bird	1,00	0,99	1,00	1,00	1,16	1,40	2,95	0,79	5,00	4,00	3,00	9,00
dog_robot	0,81	0,94	0,95	0,97	0,39	0,96	1,23	0,26	7,00	7,00	4,33	5,25
dog_tiger	0,96	0,86	0,99	0,99	0,43	0,69	3,39	0,31	9,00	3,00	6,33	9,00
drone_bird	0,91	0,99	0,95	0,99	1,70	2,28	2,38	0,35	8,00	1,00	3,00	7,75
eruption	0,98	1,00	1,00	0,99	1,99	0,74	2,69	1,14	7,75	6,00	9,00	7,25
execution	0,97	0,97	1,00	0,98	1,60	0,74	4,53	1,78	7,25	7,00	7,33	8,00
feast	0,98	0,96	0,99	0,99	1,18	0,78	2,71	0,72	8,00	3,33	5,00	7,50
human_robot	0,95	0,92	0,91	0,98	0,83	0,71	2,51	0,35	7,00	7,33	4,33	9,00
knights_barbarians	0,93	0,98	0,97	0,97	0,38	0,45	0,91	0,82	8,50	3,67	5,33	7,50
market	0,92	0,98	1,00	0,98	2,28	0,37	2,00	1,01	7,75	5,33	9,00	8,75
robot_human	0,96	0,97	0,95	0,93	0,78	0,84	1,31	0,88	8,50	7,00	3,00	7,50
robot_robot	0,92	0,96	0,90	0,96	1,26	0,75	3,50	0,74	9,00	7,67	7,33	9,00
surfer	0,91	0,92	0,93	0,97	1,76	1,52	2,69	1,63	8,50	4,00	8,67	7,50
tank	0,99	0,96	1,00	0,98	0,24	0,18	1,73	1,23	7,00	4,00	7,00	7,00
tigers_zebras	0,98	0,98	0,98	0,99	0,61	0,77	0,69	0,65	8,75	4,67	8,00	9,00
Avg	0,96	0,97	0,98	0,98	1,12	0,84	2,60	0,89	7,64	4,77	6,26	7,66

Table 11. Video Prompts.

Scene	Prompt (A)	Prompt (B)
surfer	carving a wave, surfer	carving a slope, snowboarder
desert	a desert storm swirling around dunes with sand clouds and distant lightning	a snow whirlwind swirling around hills with white clouds and distant lightning
knights_barbarians	two knights fighting with swords on a foggy battlefield at dawn, surrounded by banners and fallen shields	two barbarians fighting with axes on a foggy battlefield at dawn, surrounded by banners and fallen shields
dog_tiger	a running dog crossing a grassy meadow under the bright morning sun with dust behind its paws	a running tiger crossing a grassy meadow under the bright morning sun with dust behind its paws
cooking	a cooking woman standing in a warm kitchen with steam rising from pots on the stove	a cooking man standing in a warm kitchen with steam rising from pots on the stove
drone_bird	a flying drone hovering above a mountain lake at sunset, reflecting orange light on the water	a flying bird hovering above a mountain lake at sunset, reflecting orange light on the water
climbing	man climbing on the rocks	man climbing on the buildings
city	an ancient city surrounded by stone walls and temples in the mist, with merchants walking through the gates	a future city surrounded by glass towers and neon lights in the mist, with drones flying through the gates
blacksmith	an elf blacksmith forging a sword beside a blazing furnace in a stone workshop	a dwarf blacksmith forging a sword beside a blazing furnace in a stone workshop
dino_bird	a dinosaur walking through a tropical jungle with mist and giant trees	a bird walking through a tropical jungle with mist and giant trees
dog_robot	a running dog animal sprinting along a dirt path in the park under the morning light	a running dog robot sprinting along a dirt path in the park under the morning light
feast	a western king feasting with his men in a great hall filled with torches and banners	an oriental sultan feasting with his men in a great hall filled with torches and banners
execution	the execution of a human criminal by hanging in a medieval square at night, epic, atmospheric, filmic, 35mm lens, high dynamic range, muted color palette	the execution of a werewolf by hanging in an ancient tower, at night, epic, atmospheric, filmic, 35mm lens, high dynamic range, muted color palette
eruption	the eruption of a terrestrial volcano spewing ash and fire high into the smoky sky	the eruption of an underwater volcano spewing bubbles and lava deep beneath the sea
market	a ancient Roman market full of merchants, stalls, and peasants under the bright summer sun	a cyberpunk market full of merchants, stalls, and androids under the bright neon lights
apartment	an apartment furnished in the retro style with patterned wallpaper and wooden furniture	an apartment furnished in the modern style with smooth walls and metal furniture
chimney	a five-chimney manufacture emitting smoke over the river beside the old bridge	a five-chimney ship emitting smoke over the sea beside the old pier
tigers_zebras	seven tigers running in a circle on the dusty ground of the arena, roaring and shaking the sand	seven zebras running in a circle on the dusty ground of the arena, neighing and shaking the sand
tank	a tank drives across the meadow under gray clouds with grass flying under its tracks	a tank drives across the tundra under gray clouds with snow flying under its tracks
robot_human	a human boxer and a human karatist fighting in a bright ring surrounded by a cheering crowd	a robot boxer and a human karatist fighting in a bright ring surrounded by a cheering crowd
human_robot	a human boxer and a human karatist fighting in a large arena lit by spotlights and cameras	a human boxer and a robot karatist fighting in a large arena lit by spotlights and cameras
robot_robot	a human boxer and a human karatist fighting under rain in a dark urban courtyard	a robot boxer and a robot karatist fighting under rain in a dark urban courtyard
car_carriage	a man getting into a sport car on a rainy street beside glowing shop signs at night	a man getting into a carriage on a rainy street beside glowing shop signs at night

Table 12. 3D Prompts.

Scene	Prompt (A)	Prompt (B)
ant	realistic glossy red-black ant with segmented body, slender legs, detailed mandibles, subtle surface reflections, sculpted chitin texture everywhere	realistic crab with broad shell, extended legs, articulated claws, polished wet carapace, intricate ridges and speckled coloration
bike	modern lightweight bicycle frame, thin metal tubes, two large spoked wheels, detailed chainset, ergonomic saddle, textured rubber tires	sleek touring motorcycle chassis, prominent fuel tank, twin large wheels, exposed engine components, padded seat, patterned rubber tires
bird_dino	graceful bird, layered feathers, slender legs, defined beak, subtle color gradients and soft sheen	athletic bipedal dinosaur with balanced tail, muscular legs, short forearms, patterned scales, pronounced snout, nuanced earthy coloration overall
car	compact modern car with four doors, defined headlights, sculpted panels, reflective windows, detailed wheels and metallic paint	ornate enclosed carriage cabin with curved roof, carved panels, large wooden wheels, metal fittings, plush visible interior details
dwarf_minotaur	stocky armored dwarf standing firmly, braided beard, heavy pauldrons, layered mail, thick boots, decorative belt, polished metal accents	towering muscular minotaur upright, bovine head with horns, broad chest, leather harness, bracers, digitigrade hooves, scarred hide overall
gopher	bipedal gopher standing upright on hind legs, small paws, short tail, dense fur with subtle striping	bipedal athletic kangaroo balanced on powerful hind legs, elongated tail, compact torso, small forepaws, smooth fur showing muscle definition
horse_skeleton	elegant horse standing with arched neck, musculature, flowing mane, sturdy legs, detailed hooves, glossy coat with subtle shading	detailed horse skeleton, articulated skull, vertebrae, ribcage, slender leg bones, realistic bone texture and weathering
lego	four-legged mammal with elongated body, expressive head, defined muscles, smooth skin, subtle color transitions, harmonized organic proportions	blocky four-legged lego animal built from interlocking bricks, simplified head, jointed legs, visible studs, bright contrasting colors, playful proportions
magnolia	a mature magnolia tree with thick twisting trunk, broad branching crown, glossy dark leaves, large creamy layered blossoms	a graceful sakura tree with slender curving trunk, spreading branches, delicate pink blossoms, textured bark, emerging green leaves
marine_gen2	realistic armored space marine in powered exosuit, segmented pauldrons, reinforced gauntlets, glowing visor, futuristic rifle	realistic World War Two infantry soldier in worn field uniform, boots, strapped gear, steel helmet, bolt-action rifle
mermaid	a woman with the upper body of a human and the lower body of a fish with flowing scaled tail, defined torso, long wavy hair, shell jewelry, shimmering skin, graceful	a detailed seahorse with arched body, long tail, elongated snout, fins, mottled orange markings
robot_gen2	a middle-aged man standing upright, relaxed shoulders, arms at sides, fitted shirt, trousers, belt, neat hair, expressive face	a humanoid robot standing upright, articulated joints, arms at sides, segmented limbs, illuminated sensors, chest plating, mechanical head
ship	an atakebune warship with wooden hull, towering plank walls, roofed central structure, reinforced beams, decorative crests, shielded deck	a modern yacht with streamlined fiberglass hull, elevated deck lounge, tinted windows, stainless railings, polished fittings
temple	a Gothic cathedral with pointed arches, vaulted ceilings, flying buttresses, traceried windows, intricate stone sculptures, portals	a monumental Hindu temple with tiered shikharas, carved pillars, ornate mandapa hall, sculpted deities, decorative friezes, stone plinth
throne	a simple wooden chair with four straight legs, flat square seat, vertical slatted backrest, worn edges, visible grain	an elaborate Gothic throne with high pointed backrest, carved tracery, finials, cushioned seat, lion armrests, base, gilded accents